

Journal of Materials Chemistry A

Accepted Manuscript



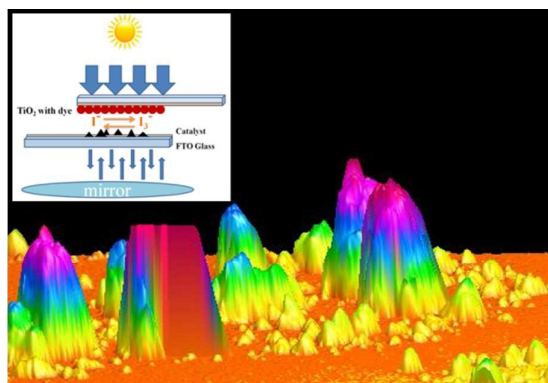
This is an *Accepted Manuscript*, which has been through the Royal Society of Chemistry peer review process and has been accepted for publication.

Accepted Manuscripts are published online shortly after acceptance, before technical editing, formatting and proof reading. Using this free service, authors can make their results available to the community, in citable form, before we publish the edited article. We will replace this *Accepted Manuscript* with the edited and formatted *Advance Article* as soon as it is available.

You can find more information about *Accepted Manuscripts* in the [Information for Authors](#).

Please note that technical editing may introduce minor changes to the text and/or graphics, which may alter content. The journal's standard [Terms & Conditions](#) and the [Ethical guidelines](#) still apply. In no event shall the Royal Society of Chemistry be held responsible for any errors or omissions in this *Accepted Manuscript* or any consequences arising from the use of any information it contains.

Graphical Abstract



The 3D CNTs/graphene CEs with different transmittance are prepared using spraying method based on CNTs/graphene (MCG) aerogels. Re-harvesting the light increases the efficiency of the DSSCs, and the cell based CE with the transmittance of 30 % obtain the highest efficiency (7.70 %).

Light Re-harvesting and Enhanced Efficiency of Dye-sensitized Solar Cells Based 3D-CNT/graphene Counter Electrodes

Jie Ma^{a*}, Wei Shen^a, Cheng Li^a, Fei Yu^{a, b*}

^{a*} State Key Laboratory of Pollution Control and Resource Reuse, School of Environmental Science and Engineering, Tongji University, 1239 Siping Road, Shanghai 200092, P. R. of China.

Tel: 86-21-6598 1831; E-mail: jma@tongji.edu.cn

^b College of Chemistry and Environmental Engineering, Shanghai Institute of Technology,

Shanghai 2001418, China; E-mail: fyu@vip.163.com

Abstract

3D multi-walled carbon nanotube (CNT)/graphene counter electrodes (CEs) with different transmittance are prepared using spraying method based on CNTs/graphene (MCG) aerogels. Fragments of MCG aerogels form 3D structure on FTO as CEs, which have shown excellent performance in DSSCs. A mirror is set under the testing cells to reflect the light passed through the counter electrodes. With the increasing loading of materials at CEs, the transparency decrease and the electrocatalytic activities improved. The conversion efficiency of these CEs based DSSCs surpassed the Pt CE (6.90 %) when the transmittance below 30 % at 662 nm, and the efficiency is as high as 7.62 % at the transmittance of 11 %. A mirror was set under the cells, the improvement of photocurrent density depended on the transmittance of the CEs. Re-harvesting the light increases the efficiency of the DSSCs, and the CE-based cell with the transmittance of 30 % obtain the highest efficiency (7.70 %).

Introduction

Dye-sensitized solar cells (DSSCs) have been regarded as a potential alternative to silicon-based solar cells due to their low cost, easy fabrication, and fine conversion efficiency¹⁻³. Typical DSSCs comprise a TiO₂ coated with dyes on a transparent conductive oxide layer as the photoanode, a redox couple as the electrolyte, and platinum (Pt) on the FTO substrate as a counter electrode (CE). With high conductivity and catalytic activity, Pt has shown excellent CE characteristics^{4, 5}; however, the high cost of precious metals has caused many researchers to focus on carbon materials with similar properties, such as carbon black⁶, carbon nanotubes (CNTs)⁷⁻¹⁰, nanocarbon^{11,12}, and graphene¹³.

To achieve new kinds of CEs for DSSCs, carbon nanotubes (CNTs) and graphene have been combined to design CEs with excellent conductivity and catalytic properties¹⁴⁻¹⁷. Furthermore, three-dimensional (3D) structure counter electrodes with graphene have exhibited great superiority in new types of CEs, such as graphene sheet with honeycomb-like structure¹⁸; hierarchical, vertically oriented graphene¹⁹; nitrogen-doped graphene foams²⁰; and p-doped graphene nano-networks²¹. Besides improving the material characteristics of CEs^{21, 22}, other parts of DSSCs also have been developed to accomplish higher conversion efficiency, reduce cost, and achieve greater stability. The redox of Co(III)/Co(II) as an electrolyte could significantly increase the open-circuit voltages (V_{oc})²³.

There are mainly two components concerning the light-harvesting property of DSSCs, the dye and the mesoporous photoanodes which supports the sensitizer²⁴. Increasing the range of absorption band is a matter of concern for the effective utilization of the solar spectrum. Many trials have been accomplished by the development of new dyes (N3 to N719, and black dyes) to increase the light re-harvesting^{25, 26}. Hardin et al.²⁷ reported luminescent chromophores were added into liquid electrolyte to absorb high-energy photons and efficiently transfer the energy to dye, increasing the absorption bandwidth of the DSSCs.

One-dimensional nanostructures are used as photoanodes to take advantage of

the large surface area to improve light harvesting²⁸; However, apart from the design of the DSSCs' inside components, improving the harvesting light from counter electrodes is also an effective way to improve the power conversion efficiency (PCE)²⁹. Maximizing the use of the incident solar light could increase the current and maximize the PCE³⁰. Previous works have primarily focused on Pt-related counter electrodes because of their high transparency^{29, 31, 32}; for carbon-material-based counter electrodes, these studies stopped at the discussion of the transmittance and thicknesses of CEs that influenced the PCE³³⁻³⁶, and thus the research on the re-harvesting light from carbon material CEs remains insufficient, the related work have been seldom reported.

Graphene/CNTs transparent electrodes have attracted enormous interest in solar cells³⁷ and field effect transistors (FETs)³⁸, the optical transmittance and sheet resistance of graphene/CNTs transparent films can be manipulated by the addition of CNTs. Peng et al.³⁹ prepared transparent, conductive, and flexible graphene/CNTs hybrids with two three-dimensional microstructures. Jiang et al.⁴⁰ reported that graphene/CNTs films were printed on flexible plastic substrates using a printing method. In this paper, graphene was selected as the dispersing agent and cross-linking agent to decorate CNTs to form a 3D-CNT aerogel. Furthermore, an island-like structure formed on the FTO substrate using the spraying method, which led to graphene/CNTs transparent films with different transmittance.

Here, we discuss light re-harvesting in CNT/graphene (MCG) CEs with different transmittance. A mirror was set under the testing cells to reflect the light passing through the counter electrodes. CNT/graphene aerogels formed by taking advantage of the self-assembling ability of graphene oxide (GO) with a reducing agent under heating. Fragments of MCG aerogels formed a 3D structure on FTO as CEs. The transmittance of CEs decreased as the load of materials increased, further influencing the electrocatalytic activities. The improved PCE resulted from the enhanced harvesting of light, MCG-CEs showed the highest PCE 7.7% at a transmittance of 30% at 662 nm with the assistance of a mirror in our experiment.

Experimental Section

Preparation of the MCG aerogels

GO solution ($1 \text{ mg}\cdot\text{mL}^{-1}$) was prepared by dissolving 100 mg of graphite oxide powder in 100 mL of distilled water for 4 h in an ultrasonic bath, with several minutes of probe sonication. Then, 400 mg of CNTs were added to the 100 ml GO solution and stirred; after 1 h of ultrasonication, the CNT/GO solution was prepared. Then, 200 mg of glutathione were added to CNT/GO solution. The CNT/GO hydrogel was created after heating the previous solution in a $95 \text{ }^\circ\text{C}$ water bath for 12 h. The aerogel was prepared by freeze-drying the hydrogel for 48 h to remove the water. Finally, the aerogel was further treated at $800 \text{ }^\circ\text{C}$ under an Ar atmosphere for 2 h.

Preparation of the counter electrode

The aerogels were ground to a powder in an agate mortar; 100 mg of aerogel powder and 20 mg of PVPk30 were dispersed into 1 mL of ethylene glycol and 2 ml ethanol, and the paste was prepared for 30 min in an ultrasonic bath. The resultant paste was sprayed directly onto FTO/glass with an airbrush. Controlling the spraying time achieved counter electrodes with different degree of transmission. Finally, these counter electrodes were annealed at $400 \text{ }^\circ\text{C}$ under flowing argon for 1 h.

Fabrication of the dummy cells

TiO_2 photoanodes were immersed in an N719 dye solution in dry ethanol at a concentration of $3 \text{ mmol}\cdot\text{L}^{-1}$ for 20 h at $60 \text{ }^\circ\text{C}$. The TiO_2 photoanodes and N719 dye were purchased from Dalian HeptaChroma SolarTech Co., Ltd. To assemble a DSSC cell, a $60 \text{ }\mu\text{m}$ -thick Surlyn film was used to separate the photoanode and CE, and the cell was assembled using two clamps. The iodide electrolyte, which consisted of 0.6 M 1-methyl propylimidazolium iodide, 0.1 M lithium iodide, 0.05 M iodine, and 0.5 M tert-butyl pyridine in acetonitrile, was injected into the solar cell through a hole on the back of the CE. To fabricate a symmetric dummy cell, two symmetric CEs facing each other were packaged using the same procedure.

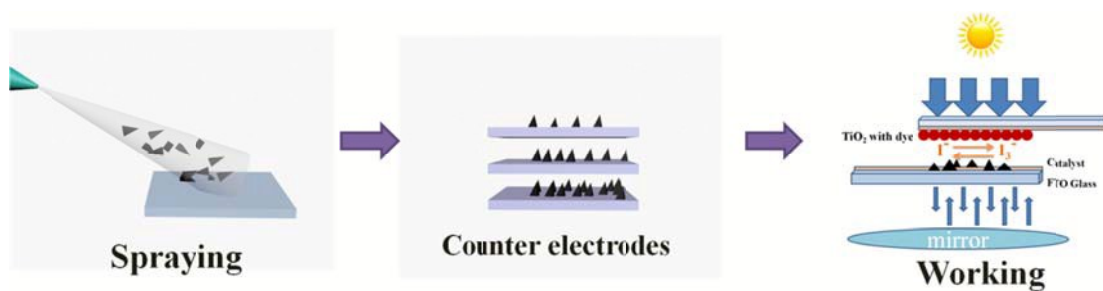
Characterization and measurements

The microstructure and morphology of the samples were analyzed using transmission

electron microscopy (TEM, JEM-2100F) and field-emission scanning electron microscopy (FESEM, Hitachi S-4800). X-ray photoelectron spectroscopy (XPS) analysis was performed in a Kratos Axis Ultra DLD spectrometer using monochromated Al K α X-rays at a base pressure of 1×10^{-9} Torr. Survey scans performed between 1,100 and 0 eV revealed the overall elemental compositions of the sample; regional scans for specific elements also were performed. The peak energies were calibrated by placing the major C_{1s} peak at 284.6 eV. Then, I-V measurements were performed using a solar simulator (91160, AM 1.5, Oriel, Newport Corporation, USA) with a power density of $100 \text{ mW} \cdot \text{cm}^{-2}$ on the surface of the test cell, and using an Oriel I-V Test Station (Model PVIV-212). This system was calibrated at NREL (USA) using an amorphous Si solar cell measurement. A silver mirror was placed under the testing cell, and used to improve the visible light utilization rate of CEs.

The cyclic voltammetry (CV), electrochemical impedance spectroscopy (EIS), and Tafel-polarization measurements were conducted using an electrochemical workstation (CHI Instruments 660D). CV was performed in the range of -0.5 to 1.0 V with a three-electrode system, Pt foil as the CE, and Ag/AgCl as the reference electrode in an acetonitrile solution containing 10 mM LiI, 1 mM I₂, and 0.1 M LiClO₄ at a scan rate of $20 \text{ mV} \cdot \text{s}^{-1}$. EIS spectra of the symmetric dummy cells were measured in a frequency range of 100 kHz to 0.1 Hz in the dark. The applied bias voltage and AC amplitude were set to 0 V and 10 mV, respectively. The EIS spectra of the symmetric dummy cells were analyzed using equivalent circuit models with Zsimpwin software. The Tafel curves of symmetric dummy cells were measured between $\pm 1.0 \text{ V}$ at a scan rate of 10 mV at room temperature. A UV-Vis spectrophotometer (UV2310 II) was used to measure the transmittances of the CEs.

Results and discussion



Schematic 1 Preparation of CE and cell testing.

Schematic 1 shows the fabrication process of different transparent CEs and the cell working model. CEs were achieved with different loading materials by controlling the spraying time. The light-harvesting was enhanced by setting a silver mirror under the cells.

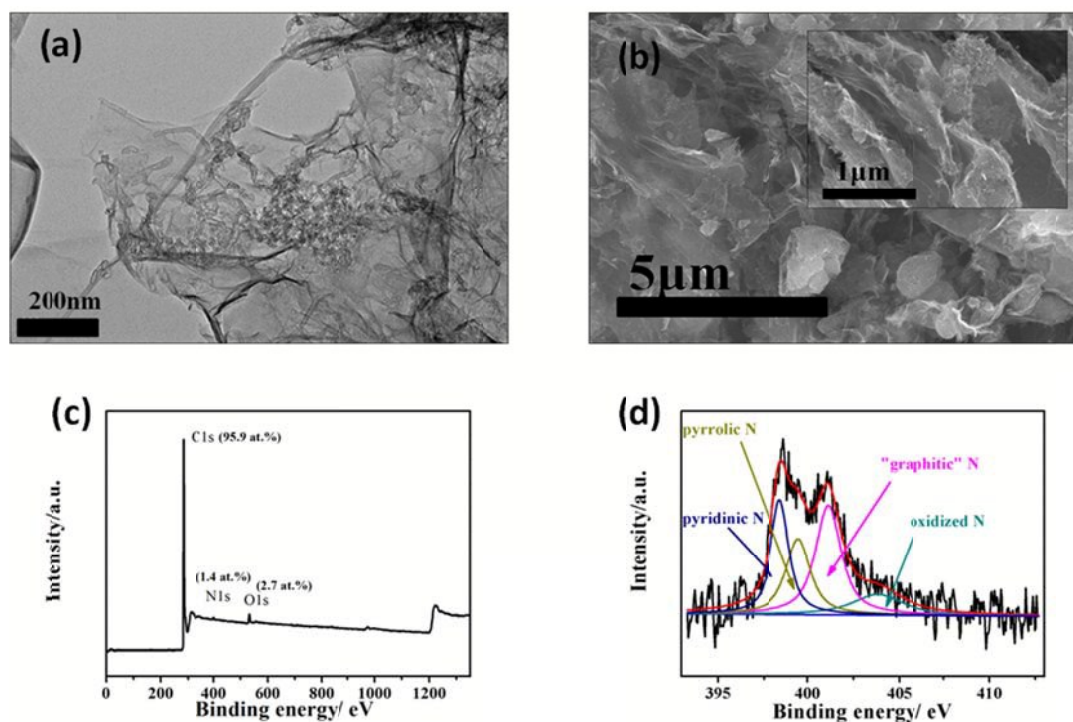


Fig. 1 TEM images (a) and SEM images (b) of MCG powders. XPS survey spectra (c) and N1s deconvolution (d) of MCG.

Fig. 1a shows the TEM image for MCG powders; wrinkled transparent graphene nanosheets combine the CNTs. Taking advantage of graphene's ability to self-assemble at high temperatures, with a reducing agent, graphene interlayer π - π stacking was the main force to form the MCG hydrogel structure. SEM images of

MCG powders are illustrated in Fig. 1b. The MCG aerogels show a highly wrinkled 3D framework, and CNTs inserted into the graphene sheets and could hardly be observed from the outside. The mass ratio of CNTs to graphene oxide is 4:1; thus, the C content of mixture would be high. Fig. 1c shows the XPS survey spectra of MCG, in which the C1s, N1s, and O1s peaks appear at 284.8 eV, 400.3 eV, and 533.8 eV, and the content of C, N, and O are 95.91 at%, 1.36 at% and 2.73 at%, respectively.

The N-doping can improve significantly the catalytic properties in the graphene⁴¹. The N_{1s} spectra of MCG can be resolved to four peaks, which imply four kinds of N species, respectively^{42,43}. As shown in Fig. 1d, the peaks appear at ~398.6 and ~399.9 eV stands for the pyridine N and pyrrole N, respectively. The N incorporated into the graphene networks is named “graphitic” N, which is located at about ~401.3eV, and the last high energy peak at ~403.8 eV is related to oxidized N. However, the pyridinic N and “graphitic” N are regarded as main catalytic active sites for iodine reduction reaction, which may be due to the shift in redox potential and the reduced adsorption energy⁴⁴.

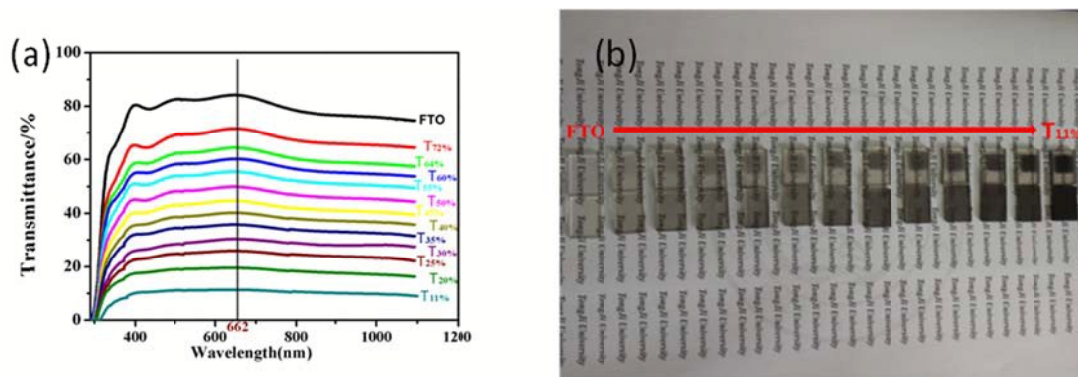


Fig. 2 UV-Vis transmittance spectra (a) and photographs (b) of counter electrodes with different transmittance.

The UV-Vis transmittance spectra of FTO and the CEs are presented in Fig. 2a. The original FTO substrate exhibits a maximum transmittance of 84.2% at 662 nm, and the Pt on FTO is 76.6 % (Fig. S1). The MCG-CEs were classified according to a different maximum transmittance at 662 nm. The CE with the highest transparency has a transmittance of 72% at 662 nm, which is labeled as T_{72%}; however, the CEs

transmitted from 71-73% were also classified as $T_{72\%}$ team in order to reduce the difficulty of the experiment. This rule was adapted to other teams. The photographs of counter electrodes with different transmittance are shown in Fig. 2b, which correspond with Fig. 2a. To further simplify the process, we chose $T_{72\%}$, $T_{60\%}$, $T_{50\%}$, $T_{40\%}$, $T_{30\%}$, $T_{20\%}$, $T_{11\%}$ CEs in the following discussion.

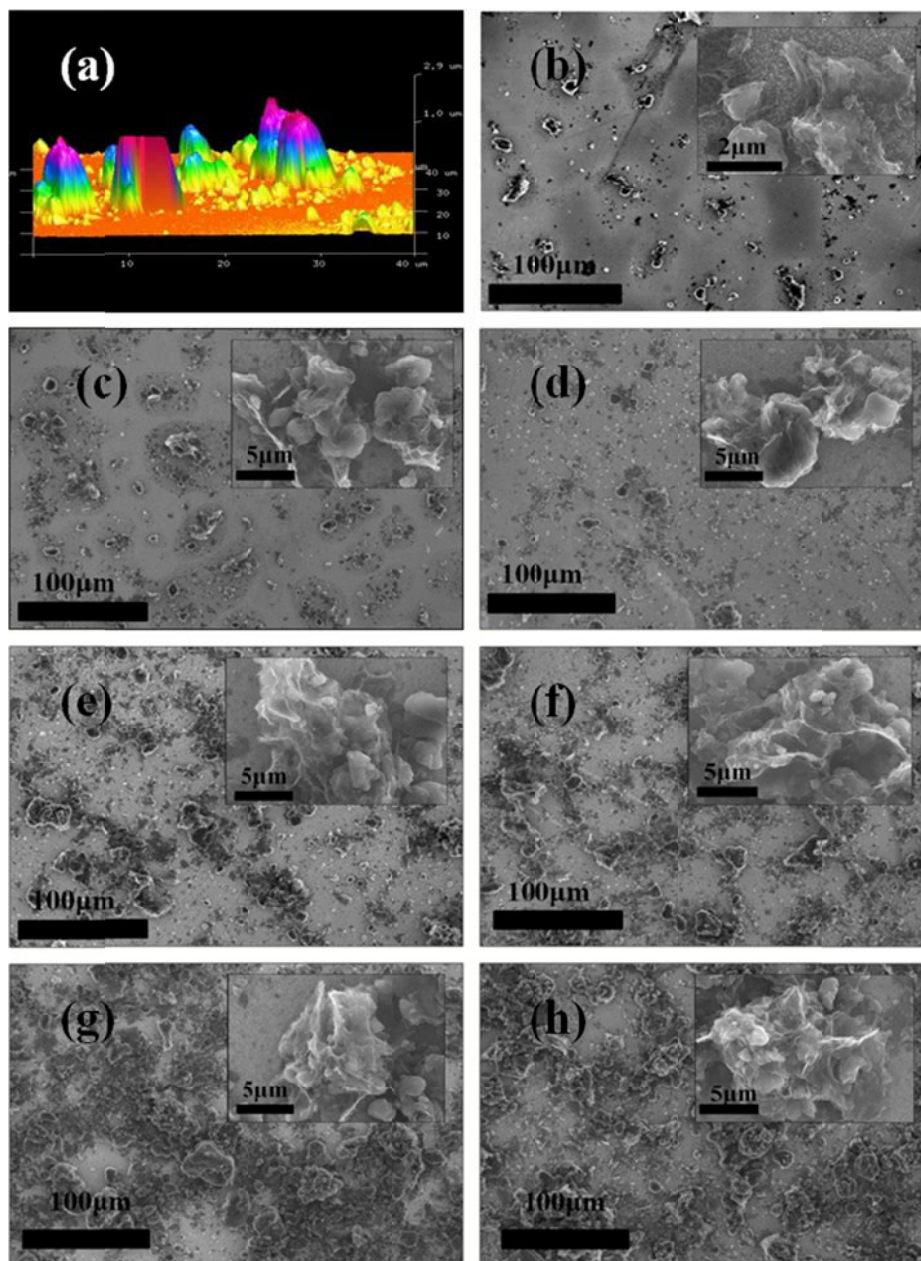


Fig. 3 AFM images (a) of the counter electrode surface, and SEM images (b-h) of counter electrodes with different transmittance at 662 nm (b $T_{72\%}$, c $T_{60\%}$, d $T_{50\%}$, e $T_{40\%}$, f $T_{30\%}$, g $T_{20\%}$, h $T_{11\%}$).

Fig. 3a presents the AFM analysis of the 3D morphology of the surface of the

counter electrode. The mountain-like morphology vividly reflects the vertical structure. The morphology analysis of CEs are illustrated in Fig. 3b-h, which are T_{72%}, T_{60%}, T_{50%}, T_{40%}, T_{30%}, T_{20%}, and T_{11%}, respectively. Obviously, the transmittance of CEs decreases as the material load on FTO increases. The size of the aerogel fragments are primarily from 10 to 20 nm, and the fragments adhere to FTO well with the help of PVPk30. Every single fragment has the 3D configuration; thus, the high coarse 3D morphology was formed with the assembly of small particles. The uncovered surface of FTO provides the certain penetrability of light and offers more space for 3D particles contacting vertically with the electrolyte.

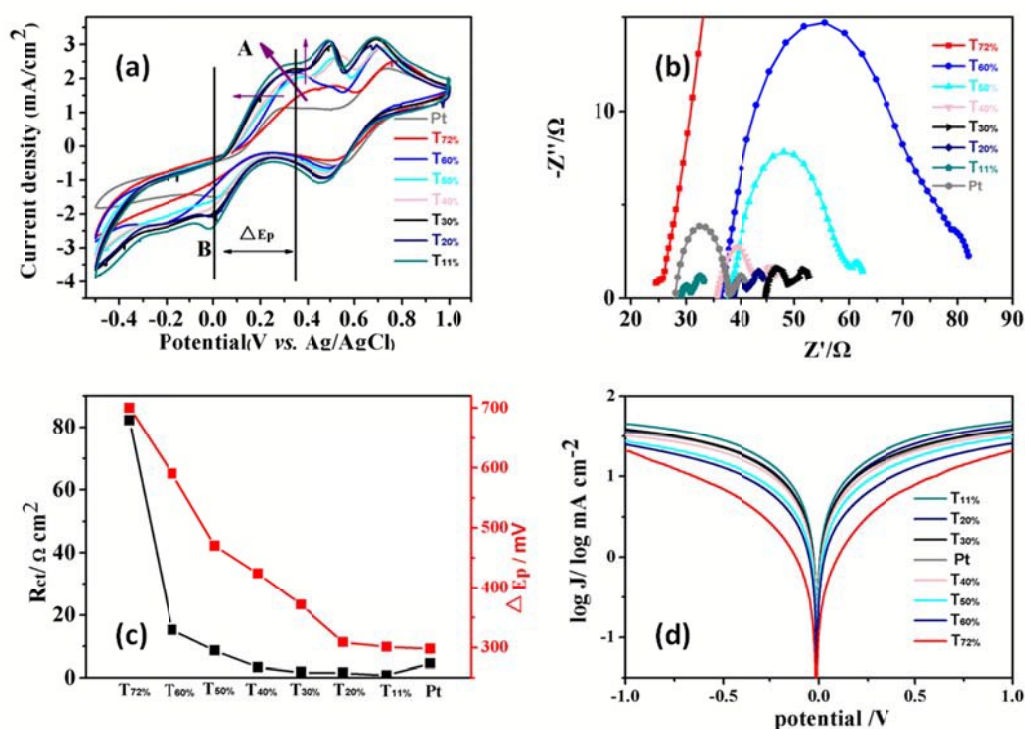


Fig. 4 Cyclic voltammograms (a) of MCG-CEs and Pt electrodes at a scan rate of $20 \text{ mV} \cdot \text{s}^{-1}$ in the Γ/I_3^- electrolyte (10 mM LiI, 1 mM I₂, 0.1 M LiClO₄, acetonitrile); Nyquist plots (b) of symmetrical dummy cells with CEs under bias 0V; (c) the value of fitted R_{ct} and ΔE_p from the previous results. Tafel plots (d) of dummy cells between $\pm 1.0 \text{ V}$ with a scan rate of 10 mV at room temperature.

To investigate the characteristics of the counter electrodes, cyclic voltammetry (CV), electrochemical impedance spectroscopy (EIS), and Tafel plots were introduced in the analysis. The electrochemical redox behavior of Γ/I_3^- of electrode was measured

through CV in a three-electrode system, with CEs as the working electrode, a Pt foil as the counter electrode, and Ag/AgCl as the reference electrode, with a scanning range from -0.5V~1.0V vs. Ag/AgCl.

The CV results are shown in Fig.4a. The pair of peaks at a relatively low potential reflects the redox reaction (1), and it is the one relevant to the functionality of the counter electrode ^{19, 45}.



The peak A of current density (J_A) and the difference in the potential value between low potential peak-to-peak separation (ΔE_p) co-decide the catalytic activity of the counter electrode. From the reaction kinetics, ΔE_p varies inversely with the charge transfer rate (k_s), indicating that the smaller ΔE_p , the better the catalytic activity ^{46, 47}. The J_A of MCG-CEs are all higher than Pt CE, implying that the 3D MCG aerogel structure could have provided more electron transport sites than the 2D-Pt CEs; thus, the MCG-CEs show good charge transfer performance. The peak A of MCG-CEs rises up while shifting to the left with the decreasing transmittance, which directly increases J_A and diminishes ΔE_p . In another words, the electrochemical characteristics of MCG-CEs increase with the loading of materials on FTO, and the additional materials could offer more reaction sites.

EIS measurement was conducted on a symmetrical dummy cell consisting of two identical electrodes; the results are shown in Fig. 4b. From the reported graphene counter electrode ²², the high-frequency semicircle between 100 kHz and 2.5 kHz reflects the Nernst diffusion impedance in the porous electrode (Z_w , pore), however, it cannot be observed in MCG-CEs EIS curves, and thus there is less coverage on the surface of the materials. In the frequency range between 25 Hz and 2.5 kHz, the impedance is related to the charge-transfer resistance (R_{ct}) and capacitance at the interface of the CE/electrolyte. R_{ct} is considered to be a crucial factor to effect power conversion efficiency. The frequency range of the serial resistance (R_{sh}) and Nernst diffusion (N_w) is consistent with classic reports ⁵. The corresponding equivalent circuit is listed in Fig. S2.

The exchange current density J_0 varies inversely with the R_{ct} , as described in Eq. 2

$$J_0 = RT / (nFR_{ct}) \quad (2)$$

where R is the gas constant, T is the temperature, n is the number of electrons, and F is the Faraday constant, and assuming an exchange current density (J_0) of $20 \text{ mA} \cdot \text{cm}^{-2}$ and the J_0 value corresponds with an $R_{ct} = 1.3 \text{ } \Omega \cdot \text{cm}^2$ ($n=1$) at room temperature⁴⁸.

The value of ΔE_P and R_{ct} are summarized in Fig. 4c. The Pt shows the ΔE_P of 298 mV and $4.5 \text{ } \Omega \cdot \text{cm}^2$. The $T_{72\%}$ have a large value of ΔE_P 700 mV and R_{ct} $82.2 \text{ } \Omega \cdot \text{cm}^2$, which reflects the poor charge-transfer ability; however, ΔE_P and R_{ct} of $T_{11\%}$ are as low as 301 mV and $0.8 \text{ } \Omega \cdot \text{cm}^2$, respectively. Therefore, the $T_{11\%}$ show excellent electrocatalytic activities, as well as exchange current density and high catalytic activity. The R_{ct} of the CEs also decrease with reduced transmittance, indicating that loading more aerogel fragments improves the catalytic activity for reducing I_3^- to I^- at the electrolyte–electrode interface. Comparing the results of the CV and EIS, the ΔE_P of MCG-CEs change in accordance with the R_{ct} , and these values are quite consistent to reflect the performance of CEs.

To further confirm the electrochemical characteristics of MCG-CEs, Tafel-polarization measurements were carried out using dummy cells as the EIS; Tafel plots are shown in Fig. 3d. The curve at intermediate potential with a sharp slope is attributed to the Tafel zone³³, and ionic diffusion coefficient D could be calculated according to Eq. (3)

$$D = 2nFcJ_{lim} / \delta \quad (3)$$

where J_{lim} is the limiting current density, n is the number of electrons in the I^-/I_3^- redox couple, F is the Faraday constant, c is the I_3^- concentration, and δ is the distance between electrodes in a dummy cell.

The limiting diffusion current density (J_{lim}) and the exchange current density (J_0) can be obtained from high potential and middle potential, respectively⁴⁹. The slopes of MCG-CEs Tafel curves become sharper with the increasing load of materials, and the Tafel zone of Pt appears between the $T_{30\%}$ and $T_{40\%}$. Larger slopes demonstrate higher exchange current density (J_0) on the surface of electrodes and indicate higher ionic

diffusion coefficient D . Results from the CV, EIS, and Tafel measurements confirm the electrocatalytic activities of MCG-CEs increase with the decreasing transmittance, and the performance is better than Pt when the transmittance of CEs is lower than 30 % at 662 nm.

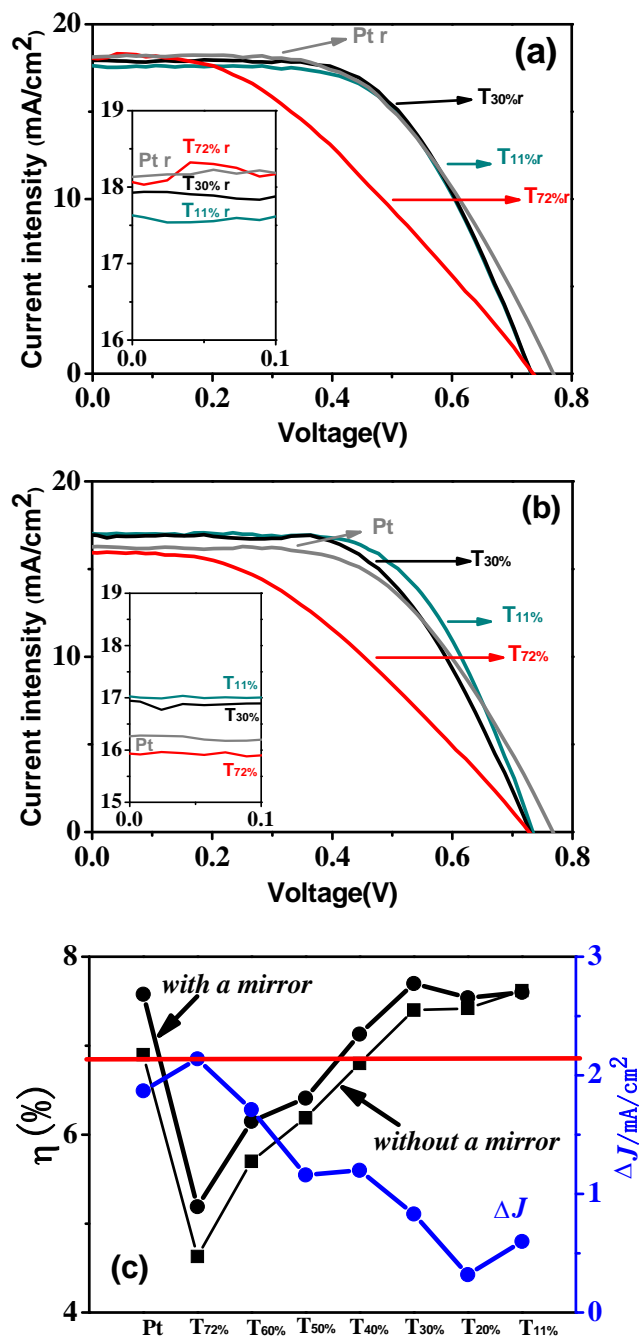


Fig. 5 Current density-voltage characteristics of the DSSCs with CEs under one sun illumination (AM 1.5G) with mirror(a) and without mirror(b); (c) the value of η and ΔJ to the corresponding cells.

Fig. 5a,b presents the photocurrent density-voltage (J-V) characteristics curves of T_{72%}, T_{30%}, T_{11%}, and Pt DSSCs under simulated solar illumination (100 mW·cm⁻², AM 1.5 G), and the corresponding curves with a mirror and without a mirror. The entire DSSCs device data is listed in Table S1. And the Fig. 5c summary the value of η and ΔJ of DSSCs. The J_{sc} improved remarkably when a mirror was set under the cells. The J_{sc} of T_{72%} increases 2.14 mA·cm⁻² and the η becomes 0.56 % higher. The J_{sc} of T_{11%} improves only by 0.6 mA·cm⁻² and the η does not change. However, the T_{30%} shows the highest η (7.70 %) with a mirror with J_{sc} increasing 0.83 mA·cm⁻². Obviously, the open-circuit voltage (V_{oc}) has little change with a mirror; therefore, reharvesting the light to increase J_{sc} (ΔJ) is the main factor for improving the η . Fig. 5c presents the curves of η and ΔJ , which clearly show the change of η with ΔJ . The η of MCG-CEs is already closed to Pt (6.9 %) at the transmittance 40 % (6.8 %) without a mirror, and the highest η is 7.62 % at T_{11%}, which is consistent with the previous electrochemical analysis results. However, the T_{30%} has higher η than T_{11%} with the advantage of light reharvesting, and this result shows the crucial significance of this work.

Conclusion

Here we fabricated different transparent CEs by controlling the spraying time, and focused on the relationship between the light re-harvesting and transmittance of CNTs/graphene CEs. Based on the CV, EIS, and Tafel results, the electrocatalytic characteristics of MCG-CEs increase with decreased transmittance; however, by re-harvesting the reflecting light from the cell with a mirror, the T_{30%}-based cell achieved a higher PCE than that of T_{11%}, although the improvement of PCE with MCG-CE-based cells is relatively lower than that of Pt due to the low transparency. Our work is important for future research on transparent CEs and the large-scale application of carbon-materials-based transparent DSSCs, such as the outside window or the outside wall.

Acknowledgements

This research was supported by the National Natural Science Foundation of China (No. 21207100, 51408362)

References

1. B. O'regan and M. Grätzel, *nature*, 1991, **353**, 737-740.
2. M. Grätzel, *Inorganic chemistry*, 2005, **44**, 6841-6851.
3. A. Yella, H.-W. Lee, H. N. Tsao, C. Yi, A. K. Chandiran, M. K. Nazeeruddin, E. W.-G. Diao, C.-Y. Yeh, S. M. Zakeeruddin and M. Grätzel, *Science*, 2011, **334**, 629-634.
4. H. Bönemann, G. Khelashvili, S. Behrens, A. Hinsch, K. Skupien and E. Dinjus, *Journal of Cluster Science*, 2007, **18**, 141-155.
5. A. Hauch and A. Georg, *Electrochimica Acta*, 2001, **46**, 3457-3466.
6. T. N. Murakami, S. Ito, Q. Wang, M. K. Nazeeruddin, T. Bessho, I. Cesar, P. Liska, R. Humphry-Baker, P. Comte and P. Péchy, *Journal of the Electrochemical Society*, 2006, **153**, A2255-A2261.
7. J. E. Trancik, S. C. Barton and J. Hone, *Nano letters*, 2008, **8**, 982-987.
8. J. Li, A. Cassell, L. Delzeit, J. Han and M. Meyyappan, *The Journal of Physical Chemistry B*, 2002, **106**, 9299-9305.
9. J. Han, H. Kim, D. Y. Kim, S. M. Jo and S.-Y. Jang, *Acs Nano*, 2010, **4**, 3503-3509.
10. J. Ma, L. Zhou, C. Li, J. H. Yang, T. Meng, H. M. Zhou, M. X. Yang, F. Yu and J. H. Chen, *J Power Sources*, 2014, **247**, 999-1004.
11. K. Imoto, K. Takahashi, T. Yamaguchi, T. Komura, J.-i. Nakamura and K. Murata, *Solar Energy Materials and Solar Cells*, 2003, **79**, 459-469.
12. X. Cai, Z. Lv, H. Wu, S. Hou and D. Zou, *Journal of Materials Chemistry*, 2012, **22**, 9639-9644.
13. W. Hong, Y. Xu, G. Lu, C. Li and G. Shi, *Electrochemistry Communications*, 2008, **10**, 1555-1558.
14. L.-H. Chang, C.-K. Hsieh, M.-C. Hsiao, J.-C. Chiang, P.-I. Liu, K.-K. Ho, C.-C. M. Ma, M.-Y. Yen, M.-C. Tsai and C.-H. Tsai, *J Power Sources*, 2013, **222**, 518-525.
15. M. Wang, Q. W. Tang, H. Y. Chen and B. L. He, *Electrochimica Acta*, 2014, **125**, 510-515.
16. H. Zheng, C. Y. Neo and J. Ouyang, *ACS applied materials & interfaces*, 2013, **5**, 6657-6664.
17. J. Ma, C. Li, F. Yu and J. H. Chen, *J Power Sources*, 2015, **273**, 1048-1055.
18. I. N. Kholmanov, S. H. Domingues, H. Chou, X. H. Wang, C. Tan, J. Y. Kim, H. F. Li, R. Piner, A. J. G. Zarbin and R. S. Ruoff, *Acs Nano*, 2013, **7**, 1811-1816.
19. K. Yu, Z. Wen, H. Pu, G. Lu, Z. Bo, H. Kim, Y. Qian, E. Andrew, S. Mao and J. Chen, *Journal of Materials Chemistry A*, 2013, **1**, 188-193.
20. Y. Xue, J. Liu, H. Chen, R. Wang, D. Li, J. Qu and L. Dai, *Angewandte Chemie*, 2012, **51**, 12124-12127.
21. H. J. Ahn, I. H. Kim, J. C. Yoon, S. I. Kim and J. H. Jang, *Chemical communications*, 2014, **50**, 2412-2415.
22. J. D. Roy-Mayhew, D. J. Bozym, C. Punckt and I. A. Aksay, *Acs Nano*, 2010, **4**, 6203-6211.

23. L. Kavan, J. H. Yum, M. K. Nazeeruddin and M. Gratzel, *Acs Nano*, 2011, **5**, 9171-9178.
24. S. K. Balasingam, M. Lee, M. G. Kang and Y. Jun, *Chem Commun*, 2013, **49**, 1471-1487.
25. M. K. Nazeeruddin, A. Kay, I. Rodicio, R. Humphrybaker, E. Muller, P. Liska, N. Vlachopoulos and M. Gratzel, *J Am Chem Soc*, 1993, **115**, 6382-6390.
26. M. K. Nazeeruddin, P. Pechy, T. Renouard, S. M. Zakeeruddin, R. Humphry-Baker, P. Comte, P. Liska, L. Cevey, E. Costa, V. Shklover, L. Spiccia, G. B. Deacon, C. A. Bignozzi and M. Gratzel, *J Am Chem Soc*, 2001, **123**, 1613-1624.
27. B. E. Hardin, E. T. Hoke, P. B. Armstrong, J. H. Yum, P. Comte, T. Torres, J. M. J. Frechet, M. K. Nazeeruddin, M. Gratzel and M. D. McGehee, *Nat Photonics*, 2009, **3**, 406-411.
28. P. Poudel and Q. Qiao, *Nanoscale*, 2012, **4**, 2826-2838.
29. Y.-L. Lee, C.-L. Chen, L.-W. Chong, C.-H. Chen, Y.-F. Liu and C.-F. Chi, *Electrochemistry Communications*, 2010, **12**, 1662-1665.
30. K. S. Lee, J. H. Yun, Y.-H. Han, J.-H. Yim, N.-G. Park, K. Y. Cho and J. H. Park, *Journal of Materials Chemistry*, 2011, **21**, 15193-15196.
31. K. M. Lee, W. H. Chiu, V. Suryanarayanan and C. G. Wu, *J Power Sources*, 2013, **232**, 1-6.
32. J.-H. Kim, D.-H. Kim, K.-P. Kim, D.-H. Jeon and D.-K. Hwang, *Thin Solid Films*, 2013, **546**, 326-330.
33. M. J. Ju, J. C. Kim, H. J. Choi, I. T. Choi, S. G. Kim, K. Lim, J. Ko, J. J. Lee, I. Y. Jeon, J. B. Baek and H. K. Kim, *Acs Nano*, 2013, **7**, 5243-5250.
34. Z. Yang, M. Liu, C. Zhang, W. W. Tjiu, T. Liu and H. Peng, *Angewandte Chemie*, 2013, **52**, 3996-3999.
35. X. Wang, L. J. Zhi and K. Mullen, *Nano Lett*, 2008, **8**, 323-327.
36. L. Kavan, J. H. Yum and M. Gratzel, *Acs Nano*, 2011, **5**, 165-172.
37. J. Ma, C. Li, F. Yu and J. H. Chen, *Chemsuschem*, 2014, **7**, 3304-3311.
38. S. H. Kim, W. Song, M. W. Jung, M. A. Kang, K. Kim, S. J. Chang, S. S. Lee, J. Lim, J. Hwang, S. Myung and K. S. An, *Adv Mater*, 2014, **26**, 4247-4252.
39. L. W. Peng, Y. Y. Feng, P. Lv, D. Lei, Y. T. Shen, Y. Li and W. Feng, *J Phys Chem C*, 2012, **116**, 4970-4978.
40. S. Jang, H. Jang, Y. Lee, D. Suh, S. Baik, B. H. Hong and J. H. Ahn, *Nanotechnology*, 2010, **21**.
41. G. Wang, W. Xing and S. Zhuo, *Electrochimica Acta*, 2013, **92**, 269-275.
42. Z. Lin, G. Waller, Y. Liu, M. Liu and C. P. Wong, *Advanced Energy Materials*, 2012, **2**, 884-888.
43. Z.-H. Sheng, L. Shao, J.-J. Chen, W.-J. Bao, F.-B. Wang and X.-H. Xia, *Acs Nano*, 2011, **5**, 4350-4358.
44. S. Hou, X. Cai, H. Wu, X. Yu, M. Peng, K. Yan and D. Zou, *Energy & Environmental Science*, 2013, **6**, 3356-3362.
45. Z. Huang, X. Liu, K. Li, D. Li, Y. Luo, H. Li, W. Song, L. Chen and Q. Meng, *Electrochemistry Communications*, 2007, **9**, 596-598.
46. X. W. Zhang, X. J. Zhang, X. Z. Zhang, Y. P. Zhang, L. Bian, Y. M. Wu, C. Xie, Y. Y. Han, Y. Wang, P. Gao, L. Wang and J. S. Jie, *J Mater Chem*, 2012, **22**, 22873-22880.
47. R. S. Nicholson, *Analytical Chemistry*, 1965, **37**, 1351-1355.
48. A. Gomez-Ramirez, V. J. Rico, J. Cotrino, A. Gonzalez-Elipse and R. M. Lambert, *Acs Catal*, 2014, **4**, 402-408.
49. M. X. Wu, X. A. Lin, A. Hagfeldt and T. L. Ma, *Angewandte Chemie-International Edition*, 2011, **50**, 3520-3524.

